CHARACTERIZATION OF SANDSTONE AND CARBONATE ROCKS USING DUAL-ENERGY X-RAY COMPUTED TOMOGRAPHY FOR SAMPLE SELECTION IN COREFLOODING TESTS

Vidal Vargas, J. A.[1]; Antelo, W. L. F.[1], Moreno, R. B. Z. L.[1]

[1] Laboratory for Oil Reservoirs (LABORE), School of Mechanical Engineering (FEM), Universidade Estadual de Campinas (UNICAMP), Cidade Universitária, Barão Geraldo, SP

Abstract. Special Core Analysis (SCAL) is vital for reservoir modelling and formulating effective exploration and production strategies. The SCAL program must select samples that accurately represent the reservoir to ensure the reliability and quality of the data obtained. Computed tomography (CT) is widely utilized in the petroleum industry as a non-destructive technique for rock characterization. This work aims to enhance sample selection for SCAL tests at different scales, by identifying lithological and petrophysical heterogeneities using dual-energy computed tomography (DECT). One hundred fourteen rock samples, comprising nine types of carbonates and five types of sandstones, each with distinct mineralogical compositions and petrophysical properties, were characterized using DECT. The samples, measuring 30 cm in length and 1.5 inches in diameter, were scanned at 130 kV and 80 kV using a medical CT scanner, generating images with a resolution of 100 × 100 × 700 µm and 512 × 512 pixels. Bulk density and effective atomic number were derived from the dual-energy data, enabling the identification of mineralogical heterogeneities and the calculation of total porosity profiles. The samples were classified into three porosity groups: low (4–7%), medium (<30%), and high (>30%). The results allowed the creation of a database of sandstones and carbonates, grouped according their main characteristics, for a more representative sample selecting for core-flooding and SCAL experiments, reducing uncertainties in the characterization of porous media and supporting the development of more accurate reservoir models.

1 Introduction

Heterogeneous porous systems challenge Special Core Analysis (SCAL) by introducing complex pore structures and mineral distributions that govern multiphase flow behavior. Variations in mineral composition (e.g., clay swelling, carbonate reactivity) alter surface wettability and adsorption, impacting relative permeability and residual trapping [1,2]. Structural heterogeneity—such as pore-size distribution and fractures—promotes preferential flow and non-uniform saturation patterns [3]. Dynamic effects such as mineral dissolution and biofilm growth modify permeability over time [4].

Advances in X-ray tomography, particularly Dual-Energy CT (DECT), provide non-destructive, high-resolution 3D imaging that quantifies these heterogeneities at multiple scales. DECT main contributions relay on simultaneously resolve mineral composition (e.g., clays, carbonates), pore distribution and fluid phases (oil/water/gas) through energy-dependent attenuation differences, enabling more accurate wettability and relative permeability predictions [5,6]. This capability allows for dynamic monitoring of fluid displacements and reactive processes under reservoir conditions, significantly improving SCAL representativeness [7]. Recent integration with machine learning further enhances predictive modelling of transport properties from pore-scale data [8], making DECT crucial for characterizing complex reservoirs and optimizing recovery strategies.

The evolution of porous media characterization has progressed through distinct technological phases, beginning with early CT applications [9] and fundamental reviews of X-ray techniques [10]. Some studies highlighted the significant advancements in characterizing porous formations using X-ray imaging and computational techniques. Al-Owihan et al. (2014) and Walls & Armbruster (2012) demonstrated the efficacy of dual-energy CT (DECT) in non-destructively analyzing conventional and unconventional cores. Analysing density and effective atomic number results made it possible to determine porosity and identify mineralogical heterogeneities within the reservoir rocks. Additionally, the studies integrated this data with geological descriptions and petrophysical logs, enhancing our understanding of reservoir heterogeneities and providing valuable insights for calibrating static and dynamic models [11,12,13].

Understanding the spatial distribution of petrophysical properties is essential for developing oil and gas fields and for predicting their performance. X-ray tomography is a non-destructive technique that provides a detailed assessment of the porosity and permeability of rock samples by visualizing the porous medium at various scales [10,11]. Representative sample selection is crucial for highly heterogeneous reservoirs, such as carbonates, with multiple porosity systems and mineralogical composition. That previous selection helps to group the samples analysis for specific goals, leading to a more

* Corresponding author: janeth@unicamp.br

sound SCAL evaluation based on the reservoir geological and petrophysical characteristics [14,15].

Based on the methodological advances presented in previous studies, this work aims to improve the sample selection for SCAL tests at different scales. Lithological and petrophysical heterogeneities are identified by combining traditional petrophysics with dual-energy computed tomography (DECT). To this end, 114 outcrop rock samples, composed of sandstones and carbonates, were characterized. The application of DECT allowed fast and accurate collection of bulk density and mineralogical composition data, resulting in a robust database supporting the strategic selection of representative reservoir samples. These results are expected to directly impact the SCAL tests quality and contribute to the future development of more reliable static and dynamic reservoir models.

2 Materials and Methods

2.1 Rock Samples

A total of 114 rock samples 30 cm long and having 1.5 inches of diameter were analyzed, comprising 45 sandstones and 69 carbonates. The samples were cleaned using a Soxhlet extractor with a combination of toluene and methanol for petrophysical characterization. Subsequently, the samples were placed in a coreholder under a confining pressure of 500 psi, and gas porosity and gas permeability were measured using a gas porosimeter and a permeability meter. The gas permeability values were adjusted to account for the Klinkenberg effect.

The sandstones are grouped into five formations: Berea Buff (BE), Bentheimer (BT), San Saba (SS), Bandera Brown, and Parker (PK). The carbonates are grouped into eight formations: Desert Pink (DP), Indiana LS 70-115 mD(ILH), Indiana LS 9-16 mD (ILL), Edwards Brown (ED), Silurian Dolomite (SD), Edwards Yellow (EY), Mt. Gambier (MT) and Wisconsin (WI).

2.2 Acquisition and Reconstruction Protocol

The images were acquired using the dual energy technique. **Table 1** describes the acquisition and reconstruction parameters used in this work.

Table 1. Dual-Energy acquisition protocol.

Parameters	High	Low
Energy (kv)	130	80
Eff. Current(mAs)	151	500
Slice (mm)	0.75	0.75
Kernels	H30s	
Slice Recon (mm)	0.7	0.7
CT scanner cooling time (min)	>10	

2.3 Total porosity and atomic number measurement using Dual-Energy technique

The procedure for measuring porosity and atomic number using DECT follows the methodology described by Siddiqui and Khamees (2004) [9], which suggests scanning three standard samples with known total density (ρ_b) and atomic number to obtain the constants of the following equations:

$$m * CTN_{low} + p * CTN_{high} + q = \rho_b \qquad \textbf{Eq. 1}$$

$$Z_{eff} = \sqrt[3.6]{\frac{r * CTN_{low} + s * CTN_{high} + t}{[0.9342 * \rho_b + 0.1759]}} \qquad \textbf{Eq. 2}$$

where m, p, q, r, s and t are constants, CTN_{low} is the low energy CT number, CTN_{high} is the high energy CT number, ρ_b is the bulk density, and Z_{eff} is the atomic number.

After solving a system of three equations with three unknowns, the values of the constants m, p, and q is obtained. With the values of the constants, the total density (ρ_b) is determined for the rock samples of interest by applying **Eq. 1**. Porosity is calculated by applying the following equation:

$$\phi = \frac{\rho_{ma} - \rho_b}{\rho_{ma} - \rho_{fluid}} \qquad \textbf{Eq. 3}$$

where ρ_{ma} is a matrix density, ρ_b is a bulk density and ρ_{fluid} is the fluid density.

The atomic number of the rock samples was determined by applying **Eq. 2** after solving the system of equations and finding the constants r, s, and t.

3 Results and Discussion

3.1 Standards Measurements

The coefficients m, p, q, r, s, and t from **Eq. 1** and **Eq. 2** were calculated using the dual energy technique to determine the total porosity and the atomic number. The CT numbers (CTN) of six samples made from different materials were measured at low (80 kV) and high (130 kV) energy levels. The H30s reconstruction algorithm was applied to derive these coefficients. The results are presented in **Table 2**.

Table 2. Density, CTN_{LOW} and CTN_{HIGH} values for homogeneous standards

Standard	ρ_b(kg/m^3)	CTN_{High}	CTN_{Low}
Air	1.2041	-1003.66	-989.05
Water	998	2.41	11.75
Peek	1305	186.31	174.61
PVC	1365	904.85	1440.97
PTFE	2153	935.02	992.24
Aluminum	2700.5	2379.09	3068.65

To select the proper three standards, required to determine the coefficients m, p, q, r, s, and t, we analyzed the correlation coefficient (R^2) between the CT numbers and

the standard densities. If the acquisition and reconstruction protocols are suitable for all the standards, the R^2 value will be close to or equal to 1. In this case, we can choose any three standards or the three standards with R^2 values close to 1. Based on this selection criterion, the air, water (DW), and aluminum (Al) standards were chosen to obtain the *m*, *p*, *q*, *r*, *s*, and *t* coefficients.

Table 3 displays the atomic number, density, and CT number values for the three selected standards. **Table 4** presents the results of the *m*, *p*, *q*, *r*, *s*, and *t* coefficients for these standards (air, distilled water, and aluminum) using H30s.

Table 3. Atomic number, density, CTN_{LOW} and CTN_{HIGH} values for selected standards

ID	ρ_b(kg/m^3)	Z_{eff}	CTN_{High}	CTN_{Low}
Air	1.2041	7.224	-1003.66	-989.05
DW	998	7.5195	2.41	11.75
Al	2700.5	13	2379.09	3068.65

Table 4. Dual-Energy coefficients for kernel H30s.

Coefficients	H30s
m	-0.9417
p	1.9275
q	1004.4248
r	30841.3880
s	-29358.9084
t	1038749.3291

By substituting the values of the coefficients *m*, *p*, and *q* into **Eq. 1**, we could determine the bulk density of the rock samples. To calculate the average porosity and the porosity profile of rock samples using **Eq. 3**, we first need the value of the matrix density ($\boldsymbol{\rho_{ma}}$). The estimated matrix density was calculated using the mineral composition of different samples and applying a calibration curve to obtain the corrected matrix density ($\boldsymbol{\rho_{maCT}}$), which can then be applied in **Eq. 3**.

3.2 Sandstones

3.2.1 Berea Buff

To calculate the average porosity and porosity profile using **Eq. 3**, we need the matrix density value of Berea Buff sandstone. This value was estimated based on the mineral composition extracted from the literature. **Table 5** displays the elemental mineralogical composition of Bandera Brown rocks.

Table 5. Mineral Composition of Berea Buff Sandstone [16].

Mineral	ρ_b (g/cm^3)	Concentration (wt%)	ρ_{ma} (g/cm^3)
Quartz	2.65	91	2.4115
Kaolinite	2.65	3	0.0795
Microline	2.56	4	0.1024
Matrix Density BE			2.5934

The matrix density must be corrected using the calibration curves (**Fig. 1**) obtained from the data in **Table 6** to calculate the corrected matrix density (ρ_{maCT}).

Fig. 2 illustrates the porosity profile of the Berea Buff sandstone samples using the H30s reconstruction algorithm. The porosity profile of the samples is relatively uniform, with values fluctuating slightly between 20% and 22%. The samples BE-2A, BE-5A and BE-9A demonstrate a consistent porosity profile, unlike others that show variations in porosity at different locations. However, an increase in porosity was noted at the sample's inlet and outlet which could be attributed to artifact effect.

Table 6. Density and CT Density for the Materials used in the calibration curve.

Material	ρ_b(kg/m^3)	ρ_{CT} (kg/m^3)
Air	1.2041	1.2041
DW	998	998
Al	2700.5	2700.5
BE-1A	2090.99	2028.98
Matrix	2593.40	**2567.28**

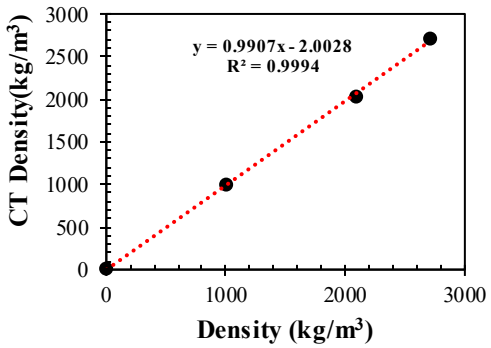

Fig. 1 Density calibration curve for the matrix density of Berea Buff Sandstone.

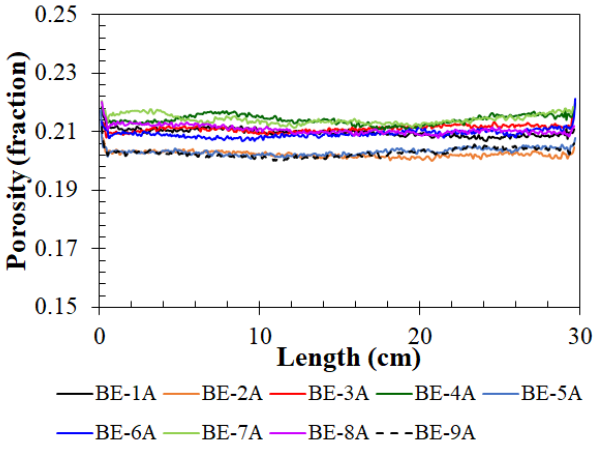

Fig. 2. Total porosity profile of Berea Buff sandstone samples.

By correlating the bulk density and atomic number of various samples on a graph, we were able to qualitatively assess the mineralogical composition of the nine

sandstones from the Berea Buff formation, as illustrated in **Fig. 3**. The data from all samples overlap, forming a line where the atomic number is approximately 12.5. The area where most of the data points cluster indicates a high quartz content, which is further supported by mineral composition. Overall, the sandstones of the Berea Buff formation exhibit nearly homogeneous petrophysical and mineralogical properties, making them ideal for conducting displacement tests.

In **Table 7**, ϕ_{gas} represents the effective porosity measured with the gas porosimeter, while ϕ_{Total_CT} indicates the total porosity determined using the dual-energy technique. By definition, total porosity is always greater than effective porosity. Therefore, we can conclude that all sample measurements provide consistent total porosity values. Sample BE-9A does not present an ϕ_{gas} measurement because it was cut before being characterized.

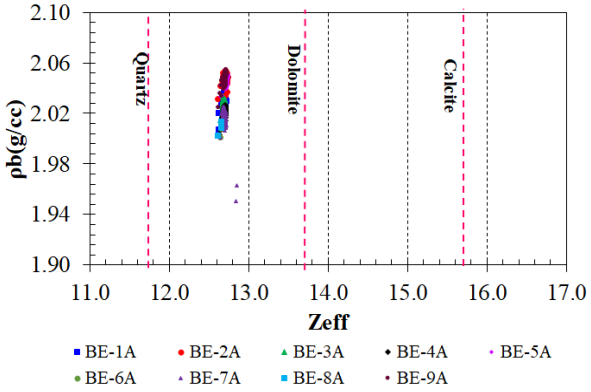

Fig. 3. Bulk density vs atomic number of Berea Buff sandstone samples.

Table 7. Effective porosity and total porosity of Berea Buff rock samples.

Sample	ϕ_{gas}(%)	$\phi_{Total_{CT}}$(%)	k(mD)
BE-1A	20.32	20.98	186.3
BE-2A	19.25	20.24	140.5
BE-3A	20.14	21.13	186.9
BE-4A	20.30	21.43	189.9
BE-5A	19.80	20.32	144.8
BE-6A	20.07	20.95	184.8
BE-7A	20.44	21.45	157.5
BE-8A	19.82	21.09	183.5
BE-9A	-	20.26	152.1

The method for calculating matrix density and then determining total porosity, as detailed in this section, will be applied to all sandstone and carbonate formations mentioned below.

3.2.2 Bentheimer

The Bentheimer (BT) sandstone consists of 91.7% quartz, 2.5% kaolinite, and 4.86% K-feldspar [17]. This mineral composition was used to determine the matrix density of the BT formation samples.

The Bentheimer sandstone samples exhibit porosities ranging from 23% to 26%, as illustrated in **Fig. 4**.

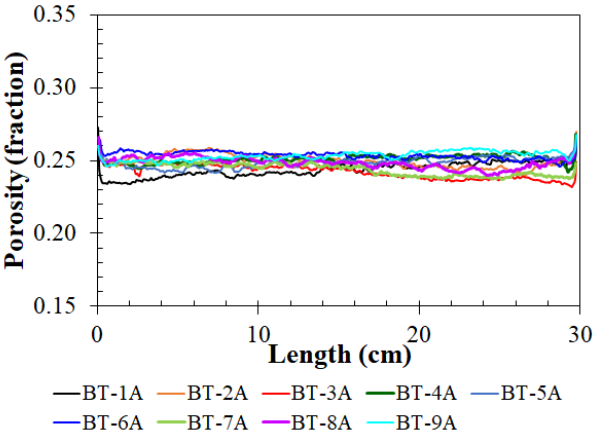

Fig. 4. Total porosity profile of Bentheimer sandstone samples.

Notably, the variations in porosity among these samples are slightly more pronounced than those found in the BE. In the first 15 cm of the samples, there is a minor variation in porosity; however, in the subsequent centimeters, the differences in porosity become more significant.

The total porosity of the Bentheimer samples increases by 7% to 15% compared to the effective porosity values, as shown in **Table 8**. According to the definition of total porosity, this difference indicates a higher percentage of unconnected pores than what is observed in Berea Buff (BE) rocks.

The mineralogical composition of BT rocks is primarily characterized by a high quartz content, along with smaller amounts of feldspars and clay minerals, as illustrated in **Fig. 5**. The data indicates clustering in the quartz region. Some points deviate from the linear trend due to higher porosity or the presence of larger amounts of feldspars or clays compared to other areas in the rock. Despite minor variations in porosity and mineralogy, Bentheimer sandstone remains an attractive candidate for coreflooding studies.

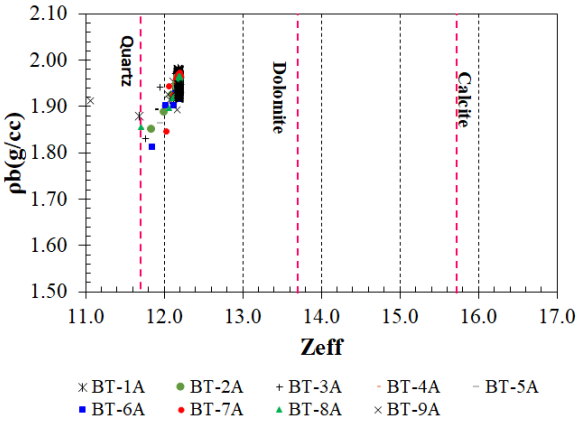

Fig. 5. Bulk density vs atomic number of Bentheimer sandstone samples.

Table 8. Effective porosity and total porosity of Bentheimer rock samples.

Sample	ϕ_{gas}(%)	ϕ_{Total_CT}(%)	k(mD)
BT-1A	22.15	24.37	1498
BT-2A	21.72	24.98	2017
BT-3A	21.54	24.25	1393
BT-4A	22.87	25.11	1931
BT-5A	21.83	24.86	1719
BT-6A	22.46	25.37	1749
BT-7A	21.71	24.40	1677
BT-8A	22.56	24.84	1663
BT-9A	23.70	25.32	1118

3.2.3 *Bandera Brown*

Bandera Brown rocks are notable for their high clay content, primarily consisting of illite. According to the Gamal. and Adebayo [18], four main minerals were identified, and the matrix density was determined. The Bandera Brown sandstone is composed of 59% (wt) quartz, 12% (wt) albite, 15% dolomite and 10% (wt) illite.

The total porosity of the BA rocks shows significant variation for a sandstone, as evidenced by the porosity profile in **Fig. 6**. The samples exhibit different profiles, with porosity ranging from 9% to 26% across the samples. This variability makes it challenging to select samples for conducting displacement tests.

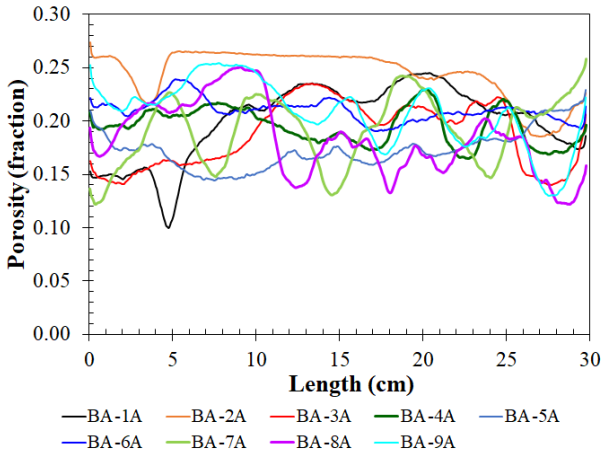

Fig. 6. Total porosity profile of Bandera Brown sandstone samples.

Table 9 presents the effective and total porosity of the BA samples. Sample BA-1A, BA-6A and BA-7A exhibit a higher effective porosity value than their total porosity. This notable difference arises because the mineralogical composition of samples BA-1A, BA-6A and BA-7A do not align with the average composition used to calculate the total porosity of the samples. Therefore, understanding the mineralogical variation of the sample is crucial for accurately determining porosity, as the matrix density value depends on this composition.

Table 9. Effective porosity and total porosity of Bandera Brown rock samples.

Sample	ϕ_{gas}(%)	ϕ_{Total_CT}(%)	k(mD)
BA-1A	23.57	20.04	3.8
BA-2A	18.75	24.42	13.9
BA-3A	18.46	18.66	5.7
BA-4A	19.35	19.56	5.0
BA-5A	16.39	17.24	0.7
BA-6A	22.80	21.00	28.7
BA-7A	20.08	19.13	4.1
BA-8A	19.44	18.35	0.4
BA-9A	18.57	20.74	3.6

The mineralogy is very diverse, as shown in **Fig. 7**. The sample data closely resemble the dolomite value, suggesting a high dolomite content.

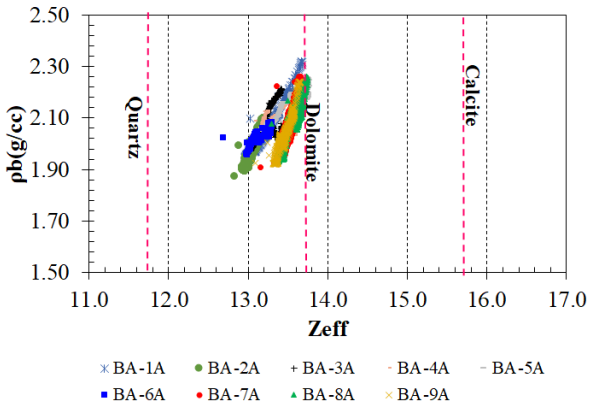

Fig. 7. Bulk density vs atomic number of Bandera Brown sandstone samples.

3.2.4 *Parker*

Quartz and clay minerals are the primary components of Parker sandstone. The mineralogical data were gathered from literature. Parker sandstone consists of 87% (wt) quartz, 5% (wt) albite, 2% (wt) kaolinite, and 4% (wt) illite [18].

The porosity distribution of the PK samples is quite homogeneous, as the profile trend is nearly linear, showing no significant variations, as illustrated in **Fig. 8**. The samples PK-1A, PK-2A, PK-5A, PK-6A, PK-8A, and PK-9A exhibit a porosity variation ranging from 18% to 19%. In contrast, samples PK-4A and PK-7A demonstrate a slight variation of 17% to 17.5%. Rock PK-4A has a high porosity value, recorded at 20%.

Fig. 9 illustrates the relationship between bulk density and the atomic number of Parker rock samples. In **Fig. 9**, the points are clustered within a narrow bulk density range, indicating a linear relationship with porosity. Additionally, the data closely aligns with the quartz zone, highlighting that quartz is the primary mineral component of this sandstone. However, despite the sandstone's uniform characteristics in terms of porosity and mineralogy, they are unsuitable or represent a challenge for displacement tests due to their very low permeability and significant clay content.

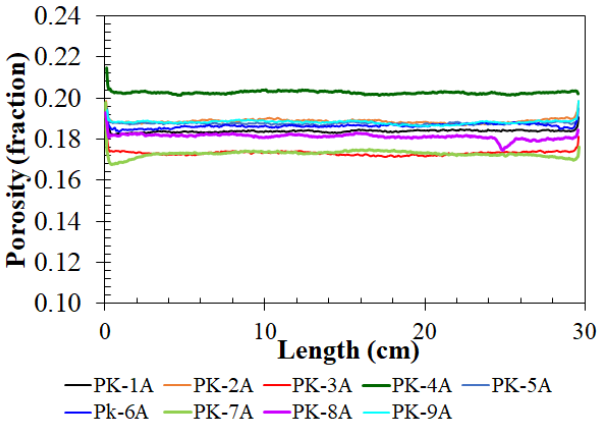

Fig. 8. Total porosity profile of Parker sandstone samples.

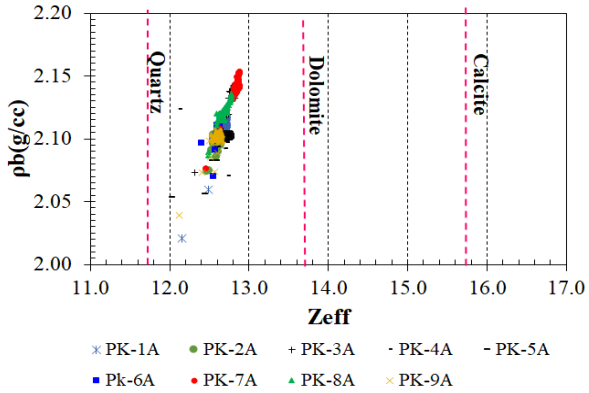

Fig. 9. Bulk density vs atomic number of Parker sandstone samples.

Table 10 displays the effective and total porosity data for the Parker samples. The total porosity values for the PK-1A and PK-7A samples show lower effective porosity, which may be due to inconsistencies in the matrix density. However, the composition of these rocks needs to be either recalibrated or obtained through experimental methods.

Table 10. Effective porosity and total porosity of Parker rock samples.

Sample	ϕ_{gas}(%)	$\phi_{Total_{CT}}$(%)	k(mD)
PK-1A	19.11	18.42	8.7
PK-2A	17.46	18.88	14.7
PK-3A	16.12	17.33	1.5
PK-4A	20.18	20.27	4.9
PK-5A	17.28	18.79	15.7
PK-6A	17.45	18.66	13.3
PK-7A	17.45	17.30	1.4
PK-8A		18.14	
PK-9A		18.83	

3.2.5 San Saba

The mineralogical composition of San Saba sandstone consists primarily of 92.7% quartz, 2.4% microcline, 2.4% albite, and 0.9% illite [19].

The San Saba sandstone's porosity distribution is homogeneous and linear, with an average value of 20%, as shown in **Fig. 10**. However, two samples, SS-7A and SS-8A, exhibit lower porosity peaks of 16% and 15%, respectively. In contrast, the porosity profile of sample SS-2A shows a higher average value of 22%. Additionally, samples SS-3A, SS-4A, SS-5A, and SS-9A each display smaller porosity peaks, approximately 19%.

The average effective porosity of San Saba rocks is 18.27%, while the effective porosity of sample SS-2A is 21%. In contrast, the average total porosity is 20.21%, with SS-2A exhibiting a total porosity of 22.32%. Additionally, the quantity of unconnected pores in San Saba sandstone ranges from 6% to 10%. The total and effective porosity data can be found in **Table 11.**

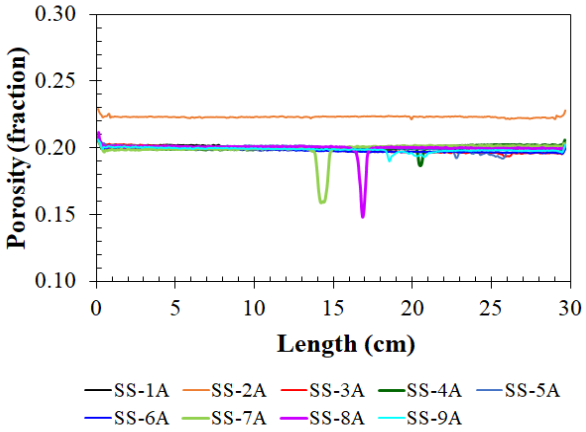

Fig. 10. Total porosity profile of San Saba sandstone samples.

Table 11. Effective porosity and total porosity of Parker rock samples.

Sample	ϕ_{gas}(%)	ϕ_{Total_CT}(%)	k(mD)
SS-1A	18.14	20.05	19.3
SS-2A	21.04	22.32	34.7
SS-3A	18.09	19.86	10.7
SS-4A	18.53	20.01	16.1
SS-5A	18.45	19.99	13.2
SS-6A	18.04	19.79	15.8
SS-7A	18.38	19.94	12.4
SS-8A		20.01	
SS-9A		19.89	

The mineralogical composition of the San Saba sandstone is consistent throughout, with quartz as the primary component, as shown in **Fig. 11**. San Saba rocks can be utilized in core flooding experiments. While their low permeability is a factor to consider, they offer the advantage of homogeneous porosity and mineralogy. San Saba rocks also contain a lower percentage of clay than Parker sandstones.

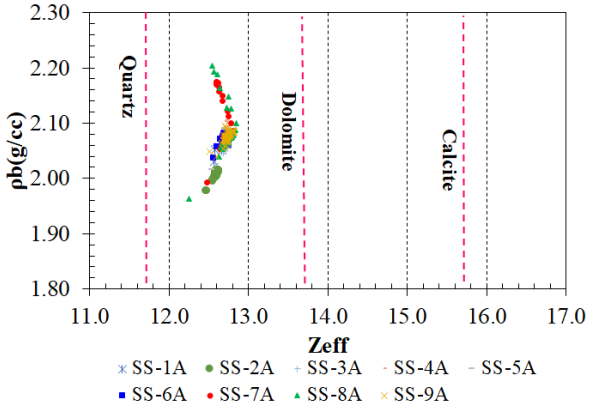

Fig. 11. Bulk density vs atomic number of San Saba sandstone samples.

3.3 Carbonates

3.3.1 Desert Pink

Desert Pink carbonate mineral composition mainly includes 80% calcite and 19.73% dolomite, along with small amounts of quartz (0.18%) and sylvite (0.09%) [20].

In **Fig. 12**, the porosity distribution of Desert Pink rocks shows a wider range of variation compared to the BE and BT sandstones. The total porosity in these rocks varies from 18% to 35%. However, the DP-7A sample exhibits a zone of low porosity, ranging from 9% to 16%. While DP rocks can be classified as heterogeneous carbonates, the porosity profile will help us select the best option for conducting displacement testing.

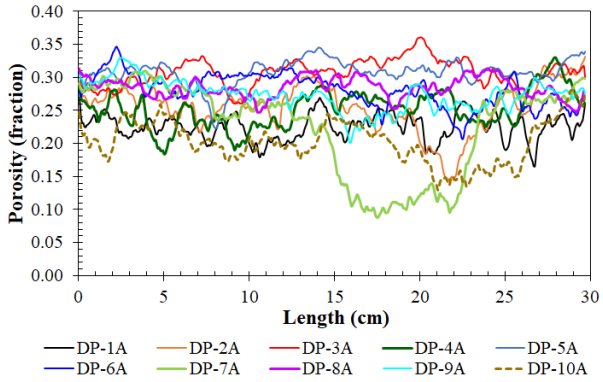

Fig. 12. Total porosity profile of Desert Pink carbonate samples.

Table 12 displays data on total porosity, effective porosity, and permeability. It is important to note that the total porosity values for samples DP-1A and DP-7A are lower than the effective porosity, which is not physically accurate. However, DP-7A demonstrates greater heterogeneity, as indicated by its wide range of porosity variation shown in **Fig. 12**.

Fig. 13 illustrates a graph of bulk density as a function of atomic number. Data variation can be observed within a range bounded by calcite and dolomite, which aligns with the mineralogy considered for this rock.

Table 12. Effective porosity and total porosity of Desert Pink rock samples.

Sample	ϕ_{gas}(%)	$\phi_{Total\ CT}$(%)	k(md)
DP-1A	26.06	22.45	22.4
DP-2A	25.32	25.42	30.9
DP-3A	29.07	30.79	32.0
DP-4A	26.08	25.26	27.7
DP-5A	30.20	30.79	38.4
DP-6A	27.55	28.07	35.6
DP-7A	24.36	22.66	14.4
DP-8A		28.47	
DP-9A		27.38	

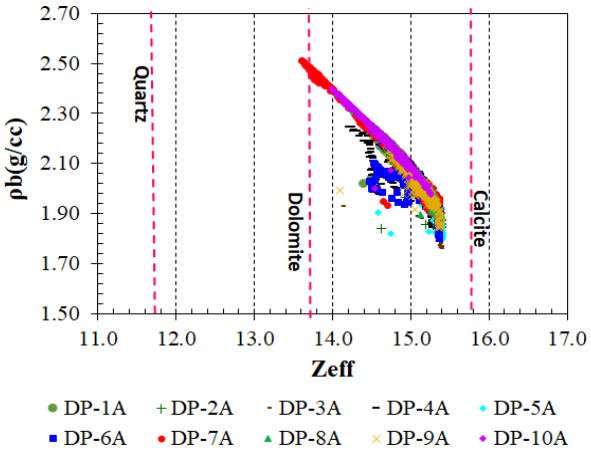

Fig. 13. Bulk density vs atomic number of Desert Pink carbonate samples.

Based on **Table 12**, **Fig. 12** and **Fig. 13**, we can conclude that DP rocks are heterogeneous due to their wide variation in mineralogy and porosity. Additionally, the permeability is found to be lower at 40 mD. The information gathered from these rocks helps us make a more representative selection of formations.

3.3.2 Indiana LS 70-115 mD

According to the study conducted by Wang et al. (2022) [21], Indiana limestone primarily consists of 98.6% calcite, along with 1.4% of other minerals. These include 0.3% quartz, 0.9% magnesium calcite, and 0.2% iron oxide. The total porosity, determined based on the matrix density, is lower than the effective porosity measured using a gas porosimeter. Additionally, an estimate of the matrix density was calculated to be ρ_{ma} = 2.870 g/cm³, corresponding to a computed tomography (CT) density of ρ_{CT} = 2.982 g/cm³.

Fig. 14 shows that the total porosity of the ILH rocks ranges from 18% to 21%. The porosity profiles indicate fluctuations, with values rising and falling within a narrow range. From this information, the ILH rocks exhibit slight heterogeneity in the porosity distribution throughout the sample.

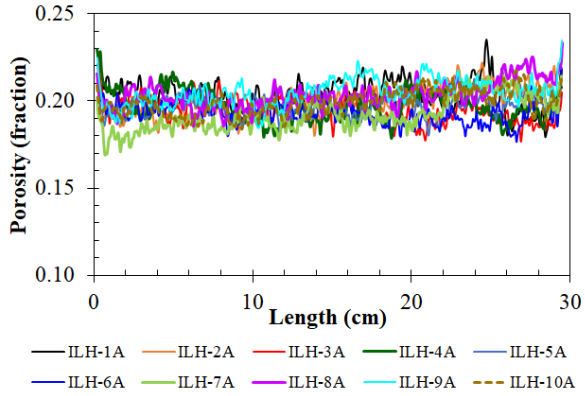

Fig. 14. Total porosity profile of Indiana LS 70-115 mD carbonate samples.

Fig. 15 illustrates that the ILH rocks have a uniform composition. The samples are significantly closer to dolomite than to calcite, which may support the hypothesis proposed for calculating matrix density.

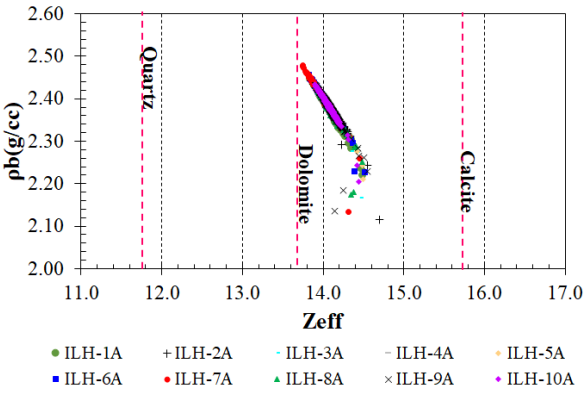

Fig. 15. Bulk density vs atomic number of Indiana LS 70-115 mD carbonate samples.

Table 13 presents the primary petrophysical properties of the ILH rocks. These rocks' permeabilities are below 30 mD. The estimated matrix density is a reliable approximation; as total porosity values exceed the effective porosity.

Table 13. Effective porosity and total porosity of Indiana LS 70-115 mD rock samples.

Sample	ϕ_{gas}(%)	$\phi_{Total_{CT}}$(%)	k(mD)
ILH-1A	19.43	20.43	28.9
ILH-2A	18.73	20.02	9.0
ILH-3A	18.09	19.57	24.2
ILH-4A	18.92	19.78	25.7
ILH-5A	19.23	19.80	25.5
ILH-6A	18.61	19.38	24.2
ILH-7A	18.56	19.27	28.6
ILH-8A	-	20.40	
ILH-9A	19.15	20.54	27.0
ILH-10A	-	19.94	

These rocks are suitable for core flooding tests, and the characteristics and measured properties can be considered for a more representative selection.

3.3.3 Indiana LS 9-16 mD

The density of the Indian LS 9-16mD matrix was estimated as ILH. Since the matrix density estimated based on the mineralogical composition reported in the literature did not give correct total porosity values. The estimated matrix density is ρ_{ma}=2.950 g/cm³ which equates to a CT density of ρ_{CT}=3.162 g/cm³.

Rocks ILL-1A, ILL-7A, and ILL-8A exhibit greater variations in total porosity throughout the sample, as illustrated in **Fig. 16**. The porosity distribution ranges from approximately 15% to 21%.

The ILL rocks exhibit a consistent composition, as the data demonstrate a linear trend and overlap, as illustrated in **Fig. 17**. Additionally, the data align with the dolomite line, suggesting that the calcite content in these rocks is relatively low compared to that of the ILH rocks.

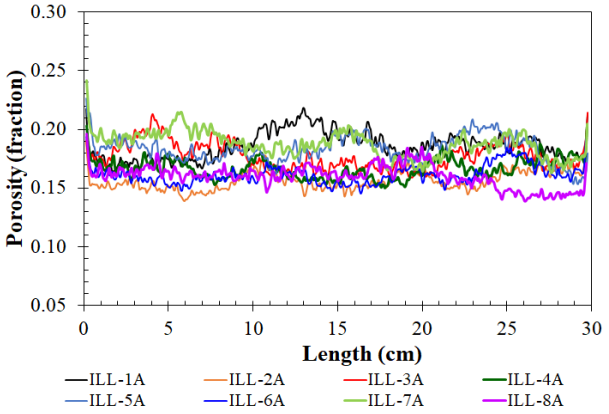

Fig. 16. Total porosity profile of Indiana LS 9-16 mD carbonate samples.

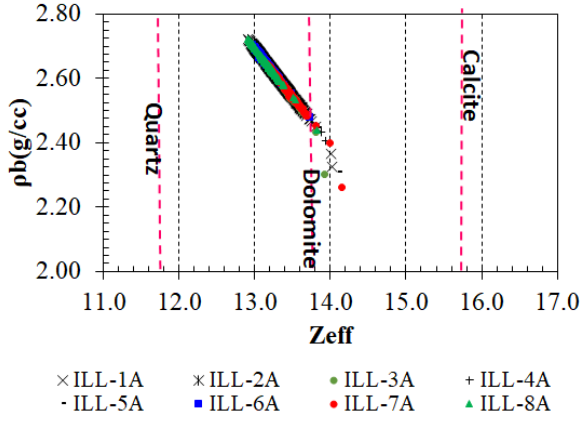

Fig. 17. Bulk density vs atomic number of Indiana LS 9-16 mD carbonate samples.

The permeability of ILL rocks is less than 10 mD, making performing displacement tests challenging (**Table 14**). The matrix density estimate serves as a good approximation, as it allows for determining total porosity values that exceed effective porosity.

Table 14. Effective porosity and total porosity of Indiana LS 9-16 mD rock samples.

Sample	ϕ_{gas}(%)	$\phi_{Total_{CT}}$(%)	k(mD)
ILL-1A	17.62	18.61	5.8
ILL-2A	12.50	15.69	6.0
ILL-3A	15.30	17.76	5.4
ILL-4A	15.12	16.68	3.8
ILL-5A	16.23	18.37	5.1
ILL-6A	14.82	16.13	5.0
ILL-7A	15.97	18.78	6.4
ILL-8A	-	16.05	

3.3.4 *Edwards Brown*

The Edwards Brown Carbonate (ED) is a type of dolomitic rock characterized as a highly porous, beige-yellow sparite. It consists predominantly of dolomite (over 90 wt%), along with silica (SiO_2) and a negligible quantity of kaolinite clay [22]. For the purpose of calculating the matrix density, ED is assumed to be composed entirely of dolomite. The estimated matrix density is $\rho ma = 2.870$ g/cm³, which corresponds to a computed tomography (CT) density of $\rho_{CT} = 2.857$ g/cm³.

Fig. 18 illustrates that the porosity of ED rocks ranges from 40% to 45%. Notably, in the first 5 cm of the ED-4A rock sample, there is a significant reduction in porosity, approximately 50%.

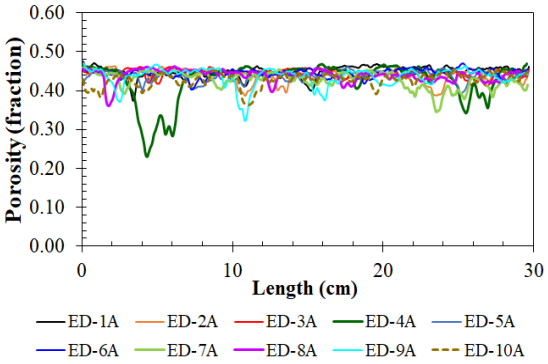

Fig. 18. Total porosity profile of Edwards Brown carbonate samples.

Table 15 presents data on effective porosity, total porosity, and permeability. The total porosity values range from 40% to 45% across the sample, while the effective porosity ranges from 40% to 43%. The porosity peaks shown in Fig. 20 correspond to vugs distributed throughout the rock's length, enhancing connectivity among them. The ED rocks exhibit permeability values greater than 270 mD, an ideal condition for conducting displacement tests.

The Edwards Brown carbonate rock exhibits a significant degree of heterogeneity both in its porous structure, characterized by the presence of vugs, and in its mineral composition, particularly due to the occurrence of sparites, especially in sample ED-4A, as depicted in **Fig. 19**. These rocks are situated within the dolomite zone, which is their primary component, as previously mentioned.

Table 15. Effective porosity and total porosity of Edwards Brown rock samples.

Sample	ϕ_{gas}(%)	ϕ_{Total_CT}(%)	k(mD)
ED-1A	43.37	44.85	340.3
ED-2A	40.69	43.89	325.6
ED-3A	40.24	44.53	356.8
ED-4A	40.52	42.63	285.5
ED-5A	40.77	43.84	276.7
ED-6A	43.16	44.50	304.5
ED-7A	40.40	42.85	362.5
ED-8A		44.00	
ED-9A	40.84	43.67	282.0
ED-10A		42.84	

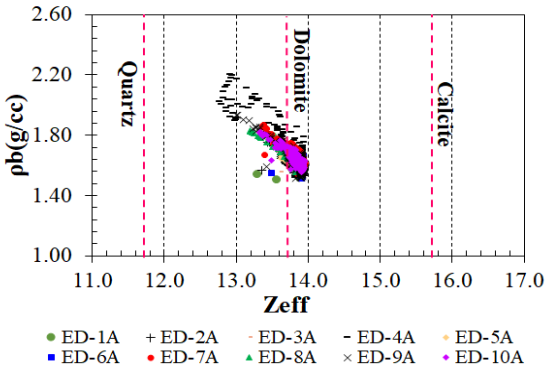

Fig. 19. Bulk density vs atomic number of Edwards Brown carbonate samples.

3.3.5 *Silurian Dolomite*

The Silurian dolomite rock primarily consists of dolomite and significant amounts of ankerite or ferrous dolomite, which can reach up to 30% in some instances [23]. However, when calculating the matrix density, it was assumed that the Silurian dolomite is composed entirely of dolomite. The estimated matrix density is $\rho_{ma} = 2.870$ g/cm³, corresponding to a CT density of $\rho_{CT} = 2.867$ g/cm³.

The Silurian Dolomite is a highly heterogeneous rock that exhibits a wide range of porosity variation among samples, as illustrated in **Fig. 20**. The total porosity varies significantly, ranging from 0% to 25%. The samples SD-4A, SD-6A, SD-8A, and SD-10A show the most pronounced variation in porosity. Some areas have zones with zero or very low porosity due to cementation or minerals with microporosity that are not detectable on the CT scale. Therefore, selecting the SD sample for displacement testing must be done carefully, as half of the SD-10A rock contains closed porosity, making flow testing impossible in the 30 cm rock section.

Table 16 presents data on effective porosity, total porosity, and permeability. The effective porosity ranges from 11% to 15%. It is important to note that the porosity of sample SD-10A is recorded as zero, which is attributed to cementation or other mineral factors that prevented

accurate measurement with the gas porosimeter. The total porosity for all samples varies between 10% and 18%. Additionally, the permeability values show significant variation, ranging from 0 to 142 mD.

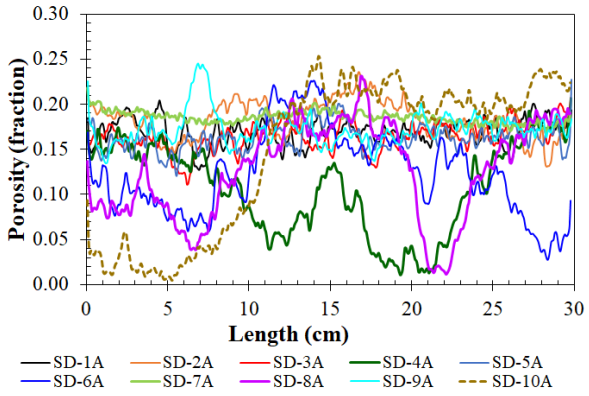

Fig. 20. Total porosity profile of Silurian Dolomite carbonate samples.

Table 16. Effective porosity and total porosity of Silurian Dolomite rock samples.

Sample	ϕ_{gas}(%)	ϕ_{Total_CT}(%)	k(md)
SD-1A	14.63	16.92	104.8
SD-2A	15.05	18.28	127.4
SD-3A	1378	16.40	67.6
SD-4A	10.91	10.73	2.1
SD-5A	14.48	16.34	75.9
SD-6A	12.84	12.35	15.1
SD-7A	15.27	18.55	141.6
SD-8A		12.69	
SD-9A	15.09	17.30	87.3
SD-10A	0.00	14.68	0.00

In **Fig. 21**, the bulk density of Silurian dolomite shows values greater than 2.1 g/cc, indicating that the rocks exhibit low porosity. Sample SD-10A demonstrates a notable variation in bulk density, ranging from 2.30 g/cc to approximately 3.00 g/cc, which also signifies low porosity. The mineral composition of sample SD is primarily dolomite, although the samples are situated in the transitional zone between quartz and dolomite.

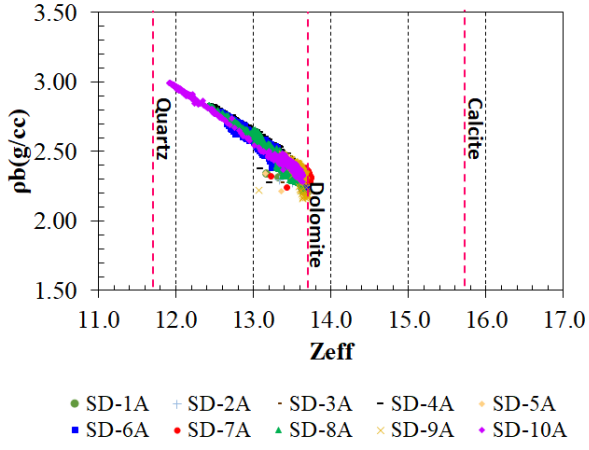

Fig. 21. Bulk density vs atomic number of Silurian Dolomite carbonate samples.

3.3.6 Mt. Gambier

The Mt. Gambier (MT) rock primarily consists of calcite and dolomite, along with smaller quantities of other minerals such as quartz, aragonite, siderite, and magnesian calcite [24]. To calculate the matrix density, it is assumed that MT is composed entirely of calcite. The estimated matrix density is ρ_{ma} = 2.71 g/cm³, corresponding to a CT density of ρ_{CT} = 2.717 g/cm³.

The porosity distribution of the MT carbonate is heterogeneous, with total porosity varying between 50% and 58%, as illustrated in **Fig. 22**. Regarding permeability, MT is reported to have values above 1D; however, the analyzed rocks demonstrated permeability values from 3 Darcy up to 12 Darcy, as shown in **Table 17.** The difference between total and effective porosity ranges from 0.9% to 2.8%, indicating the proportion of unconnected pores in the sample.

Table 17. Effective porosity and total porosity of Mt. Gambier rock samples.

Sample	ϕ_{gas}(%)	ϕ_{Total_CT}(%)	k(Darcy)
MT-1A	54.43	55.86	9.7
MT-2A	52.82	53.92	8.3
MT-3A	53.51	54.84	12.3
MT-4A	53.45	53.92	4.3
MT-5A	51.82	53.27	7.0
MT-6A	53.62	54.61	3.3
MT-7A		54.88	
MT-8A		53.49	
MT-9A		53.79	
MT-10A		53.99	

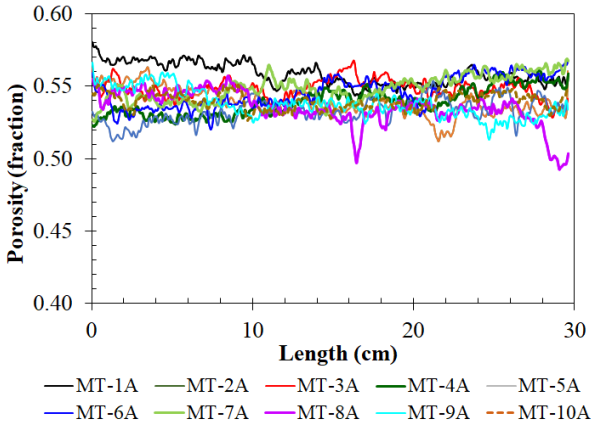

Fig. 22. Total porosity profile of Mt. Gambier carbonate samples.

The MT carbonate rock exhibits very low bulk density values, indicating that the sample has high porosity. The mineralogical composition consists mainly of a mixture of dolomite and calcite, as evidenced by the linear trend in the data distribution within the range defined by these minerals, which can be seen in **Fig. 23**.

Compared to other carbonates like SD and ILH, Mt. Gambier carbonate is optimal for displacement testing due to its high permeability and porosity.

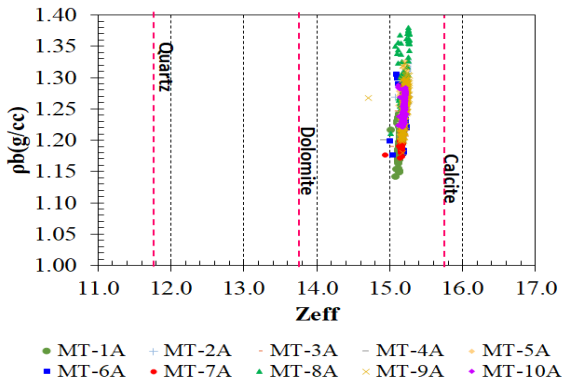

Fig. 23. Bulk density vs atomic number of Mt. Gambier carbonate samples.

3.3.7 Edwards Yellow

In the literature, Edwards yellow carbonate primarily consists of calcite. However, the matrix density was assessed, as calcite alone did not provide coherent values for total porosity. This inconsistency may arise from the mineralogy not being representative of the samples or unsuitable dual-energy acquisition parameters for this carbonate type. Consequently, it was assumed that the Edwards yellow carbonate (EY) contains 79.4% dolomite, 20% calcite, and 0.6% pyrite to determine the matrix density. The estimated matrix density is ρ_{ma} = 2.851 g/cm³, corresponding to a CT density of ρ_{CT} = 2.934 g/cm³.

Fig. 24 illustrates the total porosity as a function of position. The porosity distribution of the EY samples is highly heterogeneous, with variations ranging from approximately 15% to 27%. **Table 18** presents the average effective and total porosities and permeability values. The difference between total and effective porosity indicates the quantity of unconnected pores varying from 4% to 10%. Additionally, EY rocks exhibit low permeability, measuring less than 26 mD.

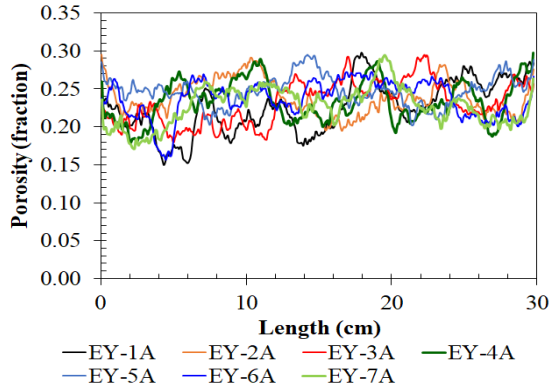

Fig. 24. Total porosity profile of Edwards Yellow carbonate samples.

Fig. 25 illustrates the relationship between bulk density and atomic number. The data displayed in this graph follow a linear trend, suggesting that the rocks have a nearly uniform mineralogical composition, as defined by the range between calcite and dolomite.

Table 18. Effective porosity and total porosity of Edwards Yellow rock samples.

Sample	ϕ_{gas}(%)	$\phi_{Total_{CT}}$(%)	k(mD)
EY-1A	21.67	22.57	6.7
EY-2A	22.52	23.87	15.0
EY-3A	21.59	23.12	12.9
EY-4A	22.27	23.39	14.1
EY-5A	22.42	24.72	25.7
EY-6A	22.13	23.71	16.1
EY-7A	21.74	22.71	16.6

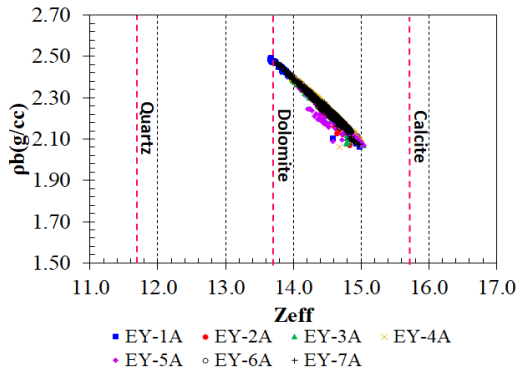

Fig. 25. Bulk density vs atomic number of Edwards Yellow carbonate samples.

3.3.8 Wisconsin

Wisconsin carbonate consists primarily of 81.93% dolomite, 1.24% feldspar, 16.17% quartz, and 0.6% calcite [20].

Table 19 displays the values for effective porosity, total porosity, and permeability. The Wisconsin carbonate exhibits very low permeability, measuring greater than 3 mD, which disqualifies these rocks from being suitable candidates for displacement tests. The effective porosity of these rocks is greater than 10%, while the total porosity is 12%.

Table 19. Effective porosity and total porosity of Wisconsin rock samples.

Sample	ϕ_{gas}(%)	$\phi_{Total_{CT}}$(%)	k(mD)
WI-1	7.80	12.70	2.9
WI-2	8.80	12.44	1.0
WI-3	8.76	12.55	2.5
WI-4	8.76	12.19	2.3

Fig. 26 illustrates the distribution of total porosity, ranging from 12% to 14%. The most significant variation is observed in the first 5 cm and the last 5 cm.

Fig. 27 illustrates the bulk density as a function of the atomic number of Wisconsin rocks. The data shown in this graph fall within the zone defined by quartz and dolomite, which aligns with the composition provided. The data do not exhibit a linear trend, suggesting that the mineralogical composition of the samples varies slightly. Additionally, Wisconsin rocks contain a significant amount of clay, which is crucial information for selecting suitable experimental tests to conduct with these samples.

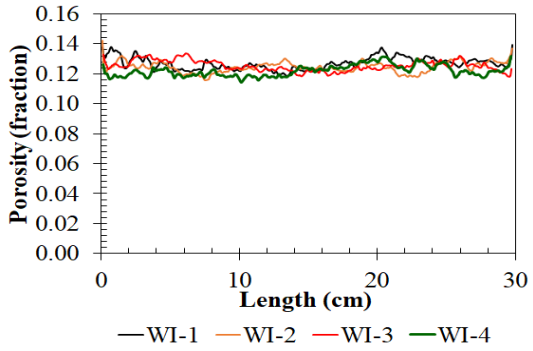

Fig. 26. Total porosity profile of Wisconsin carbonate samples.

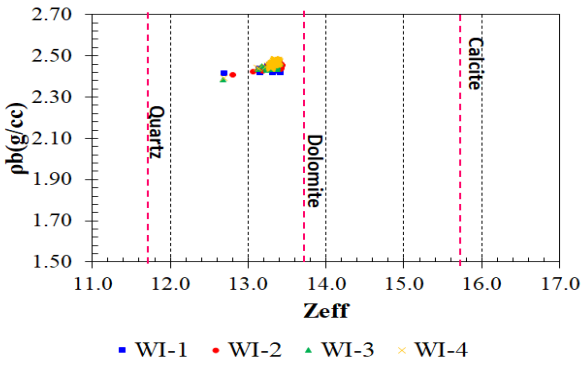

Fig. 27. Bulk density vs atomic number of Wisconsin carbonate samples.

4 Conclusions

The study involved 114 rock samples, including 45 sandstones and 69 carbonates, which were characterized using the Dual-Energy technique (DECT). This technique provided images that helped us gather crucial information for selecting the most suitable rocks for coreflooding studies or SCAL experiments. The key findings from the analysis include:

Porosity Profile: This allowed us to assess porosity distribution throughout the samples.

Bulk Density Graph: Analyzed as a function of atomic number, this graph helped us qualitatively evaluate the mineralogy of the samples.

Evaluation of Heterogeneities: By examining porosity, bulk density, and atomic number data, we identified various types of heterogeneities present in the samples, which will be useful for scaling down our studies.

Porosity Discrepancies: Differences in total porosity highlighted the importance of understanding the rocks' mineralogical composition to accurately determine the matrix's density.

Impact of Image Quality: Discrepancies in total porosity data were also attributed to the quality of the images obtained, which can affect porosity determination, as observed in the ILH and ILL samples.

This information is for guiding future research and ensuring accurate assessments in our coreflooding studies.

"We gratefully acknowledge the support and sponsorship by Equinor Brazil (Project ANP 23271-0). We also acknowledge the support of ANP (Brazil's National Oil, Natural Gas and Biofuels Agency) through the R&D levy."

Reference

1. Andersen, P. Ø., Li, X., & Standnes, D. C. (2021). *Advances in Water Resources*, 154, 103947.
2. Song, W., de Haas, T. W., & Fadaei, H. (2022). *Journal of Colloid and Interface Science*, 608(Pt 1), 505-518.
3. Bultreys, T., De Boever, W., & Cnudde, V. (2020).. *Transport in Porous Media*, 133(1), 1-31.
4. Zhang, Y., Yin, X., & Kang, Q. (2023). *Water Resources Research*, 59(4), e2022WR033456
5. Blunt, M. J., Bijeljic, B., Dong, H., Gharbi, O., Iglauer, S., Mostaghimi, P., ... & Pentland, C. (2013). *Advances in Water resources*, 51, 197-216.
6. Van Geet, M., R. Swennen, and M. Wevers (2000). *Sedimentary Geology*, 132, 25–36.
7. Iglauer, Stefan; Pentland, C. H.; Busch, Andreas (2015). *Water Resources Research*, v. 51, n. 1, p. 729-774, 2015.
8. DA WANG, Ying et al (2021). *Earth-Science Reviews*, v. 215, p. 103555, 2021.
9. Siddiqui, S., & Khamees, A. A. *In SPE Annual Technical Conference and Exhibition*, (pp. SPE-90520), (2004).
10. Cnudde, V., & Boone, M. N. *Earth-Science Reviews, 123, 1-17 (2013).*
11. Al-Owihan, H., Al-Wadi, M., Thakur, S., Behbehani, S., Al-Jabari, N., Dernaika, M., & Koronfol, S. *In IPTC Conference (pp. cp-395), (2014).*
12. Walls, J.D., and Armbruster, M.A., Rapid non-destructive analysis of unconventional cores with dual-energy CT scanning. *URTeC Conference Paper* URTEC-2012-1511485 (2012).
13. Dakshinamurthy, R., Chandrasekhar, S., Nawari, A., and Rahman, M., Computation of relative permeability curves in Middle Eastern carbonates using digital rock physics. *IPTC Conference Paper* IPTC-17636-MS (2014).
14. Hebert, V., Garing, C., Luquot, L., Pezard, P. A., & Gouze, P., 406(1), 61-79, (2015).
15. Chakraborty, R., Späth, M., Kumar, A., Busch, B., Nestler, B., Mamtani, M. A., & Hilgers, C., *Journal of Structural Geology,* 105338, (2025).
16. Shehata, A. M., & Nasr-El-Din, H. A., *SPE Reservoir Evaluation & Engineering*, *20*(01), 087-106, (2017).
17. Peksa, A. E., Wolf, K. H. A., & Zitha, P. L. *Marine and Petroleum Geology*, *67*, 701-719, (2015).
18. Gamal, H., Elkatatny, S., & Adebayo, A. (2021). *Journal of Petroleum Science and Engineering*, *202*, 108595, (2021).
19. An, B., Yan, K., Robinson, B., Hu, J., & Yuan, Q. *Applied Thermal Engineering*, *252*, 123687, (2024).
20. de Castro, L. T., Archilha, N. L., Misságia, R. M., de Ceia, M. A., Neto, I. A. L., & de Souza, F. R. (2013, August). In *EXPOGEF, Rio de Janeiro, Brazil, 26–29 August 2013* (pp. 1129-1133).
21. Wang, Y., Almutairi, A. L. Z., Bedrikovetsky, P., Timms, W. A., Privat, K. L., Bhattacharyya, S. K., & Le-Hussain, F., *Journal of Hydrology*, *614*, 128533, (2022).
22. Sadeghnejad, S., Reinhardt, M., Enzmann, F., Arnold, P., Brandstätter, B., Ott, H., ... & Kersten, M., *Advances in Water Resources*, *179*, 104501, (2023).
23. Cichon-Pupienis, A., Littke, R., Froidl, F., & Lazauskienė, J., *Marine and Petroleum Geology*, *112*, 104083, (2020).
24. Alizadeh, S. M., Latham, S., Middleton, J., Limaye, A., Senden, T. J., & Arns, C. H., Advances in Water Resources, 100, 48-61, (2017).